Scilight

The Solid-State Sensors Journal
https://www.sciltp.com/journals/sssj

Article

Characterising Next Generation Epitaxial Silicon Detectors for Microbeam Radiation Dosimetry

Andrew Dipuglia [1], Jeremy A. Davis [1,*], Jason Paino [1], Matthew J. Cameron [1], Marco Petasecca [1], Zeljko Pastuovic [2], Vladimir Perevertaylo [3], Anatoly B. Rosenfeld [1] and Michael L.F. Lerch [1]

[1] Center for Medical and Radiation Physics, University of Wollongong, Wollongong, NSW 2522, Australia
[2] Australian Nuclear Science and Technology Organisation, New Illawarra Rd., Lucas Heights, NSW 2234, Australia
[3] SPA BIT, 81 Mayakovskoho Avenue, Kyiv 02232, Ukraine
* Correspondence: jeremyd@uow.edu.au

How To Cite: Dipuglia, A.; Davis, J.A.; Paino, J.; et al. Characterising Next Generation Epitaxial Silicon Detectors for Microbeam Radiation Dosimetry. *The Solid-State Sensors Journal* **2026**, *1*(1), 1.

Received: 11 June 2025
Revised: 4 August 2025
Accepted: 8 September 2025
Published: 3 December 2025

Abstract: A next-generation p-type epitaxial single silicon strip detector, EPI37, has been developed by the Centre for Medical and Radiation Physics for dosimetry and quality assurance in synchrotron Microbeam Radiation Therapy. The sensitive volume of the dosimeter, as defined by a thin strip junction and surrounding guard ring, has dimensions of 5 × 37 × 200 μm^3. Charge collection characteristics of the device were assessed using ion beam induced charge microscopy, to characterise the actual sensitive volume size and assess the expected operational behaviour. To test the suitability of the device for use in synchrotron Microbeam Radiation Therapy, the EPI37 was used to measure pertinent characteristics of a synchrotron microbeam radiation treatment field, such as the peak-to-valley dose ratio and the full-width half-maximum. The results were compared to those using the commercially available PTW microDiamond. The results demonstrate the feasibility of the EPI37 for use in microbeam radiation therapy dosimetry.

Keywords: microbeam radiation therapy; dosimetry; quality assurance; characterisation; single silicon strip detector

1. Introduction

Microbeam Radiation Therapy (MRT) is considered a promising pre-clinical radiotherapy modality owing to its capacity to deliver spatially fractionated, high-dose radiation that effectively ablates tumour tissue while preserving surrounding normal tissue, an effect attributed to the tissue-sparing phenomenon documented in in-vitro experiments and preclinical animal studies [1–4]. The microbeam arrays exhibit a characteristic spatial dose distribution comprising high-dose “peaks” interspersed with low-dose “valleys”. Initially, third-generation synchrotron light sources were utilised for the production of MRT fields owing to the exceptional brightness and low divergence of X-rays produced by synchrotron insertion devices. Recent research in the field of MRT has utilised more compact X-ray sources to produce suitable MRT beams [5–7]. Spatial fractionation is achieved by means of a multislit collimator (MSC). The geometric design of the MSC dictates the width and center-to-center (c-t-c) spacing of individual microbeams within the array. Individual microbeams typically exhibit widths in the range of 25–100 μm, with c-t-c spacing varying between 100–400 μm. MRT is actively being investigated at facilities worldwide, with preclinical and translational studies evaluating its therapeutic potential and assessing its clinical translatability. [2,4,8–11].

As with any radiotherapy treatment, accurate Quality Assurance (QA) prior to treatment is required to ensure accurate dose delivery according to the prescribed treatment plan [12]. In comparison with traditional external beam radiotherapy modalities, there is an added layer of complexity in performing dosimetry of the microbeam

treatment field, attributed to the features that facilitate the efficacy of MRT, i.e., spatial fractionation, dose rate, etc. The key dosimetric parameters of interest in MRT are related to the structure of the microbeam array; most notably, the Peak to Valley Dose Ratio (PVDR) and the Full Width at Half Maximum (FWHM). The dose delivery within the valley must remain low enough to facilitate normal tissue repair, whilst the dose delivered within the peaks must be sufficiently high in order to have an appreciable effect. The exact valley dose required to facilitate normal tissue repair remains an active area of research; however, the proportion of normal tissue receiving valley dose below a tissue-specific threshold has been suggested as the most likely indicator of normal tissue toxicity. The complexities of the radiation environment necessitate the need for new technology, methods, and protocols [13,14] to satisfy QA requirements. Consequently, a detector used in such a protocol must have the following properties [15]:

- Large dynamic range: In order to resolve microbeam peak(s) and valley(s) simultaneously with a good signal-to-noise ratio
- High spatial resolution: Enable adequate sampling of the μm-sized microbeam peak(s) and reduce the effects of volume averaging
- High radiation hardness: Minimise the reduction in detector signal as a function of radiation damage caused by the high dose rates used in MRT
- Real-time readout: To minimise the time between measurement and result

Currently, there is a large range of high spatial resolution dosimeters that present as promising candidates for implementation in MRT dosimetry. In 2010, Brauer-Krich et al. evaluated the current status of high-resolution dosimeters investigated for use in MRT, assessing their inherent limitations and advantages [16]. In this study, it was concluded that no single dosimeter has been developed that enables measurement of absolute dose to within the accuracy requirements for radiation therapy outlined in the Institute of Physics and Engineering in Medicine (IPEM) Report 81 [17]. Moreover, the accessibility of these devices remains a critical limitation, with most prospective technologies still in the experimental or research phase and therefore not available for commercial use. The PTW microDiamond (model 60019, PTW, Freiburg, Germany) and Gafchromic™ film represent the limited range of commercial dosimeters available with spatial resolution suitable for MRT dosimetry. Radiographic film, while widely used for dosimetry, is constrained by its lengthy development process, which precludes real-time dose readout, and in the context of MRT, by its limited dynamic range. To compensate for the dynamic range of radiographic film, published protocols have utilised multiple film types to resolve both high-dose peaks and low-dose valleys independently [18,19]. Furthermore, standard flatbed scanners may not have the necessary resolution to resolve microbeam structures in the film, thus necessitating the use of microscopes to achieve sufficient resolution. This has the effect of introducing artefacts due to the granular structure of the film that introduces uncertainty into microbeam valley measurements [20]. The PTW microDiamond detector is capable of real-time readout and micrometre-sized spatial resolution. If the microDiamond is perfectly aligned with the central axis perpendicular to the beam direction, the detector should be able to achieve a resolution of 1 μm. However, in order to avoid geometric effects that would degrade the spatial resolution, a lengthy and difficult alignment process is often required [21]. This process can be expedited utilising a method as described by Davis et al. of aligning the PTW microDiamond detector rapidly in real-time, minimising the otherwise lengthy alignment process [22].

Silicon Single Strip Detectors (SSDs) have been the subject of investigation by the Centre for Medical Radiation Physics (CMRP) at the University of Wollongong for several years [23–27]. The devices are designed for integration with the high-speed data acquisition platform developed by the CMRP, the X-ray Treatment Monitoring System (X-TREAM), and constitute a promising technology for implementing QA protocols in MRT [24,25,28]. An initial SSD prototype implementing a 50 μm thick epitaxial layer (EPI50) was previously characterised; however, the size of the sensitive volume (SV) of the device was identified as a limiting factor when performing dosimetry of small MRT fields [24,25]. A next-generation p-type epitaxial SSD has been developed to address the complications in dosimetry of synchrotron-based MRT, as well as improve on the shortcomings of the previous generation device. The fabricated dosimeter, henceforth known as EPI37, was designed at CMRP and produced by SPA-BIT (Kiev, Ukraine) as an alternative SSD prototype to the EPI50.

In this study, an Ion Beam Induced Charge (IBIC) collection analysis was conducted to characterise the sensitive volume of the fabricated devices, evaluate their expected operational behaviour, and quantify their sensitivity under varying operational configurations. Furthermore, preliminary performance testing of the EPI37 detectors in a spatially fractionated radiation field representative of MRT was carried out at the Imaging and Medical Beam Line (IMBL) of the Australian Synchrotron, with results compared to those obtained from a PTW microDiamond detector and the previously characterised EPI50 device. The SV of the EPI37 detectors was verified

in both edge-on (detector surface parallel to the beam direction) and face-on (detector surface perpendicular to the beam direction) orientations, as shown in Figure 1, to assess the spatial resolution achievable in each configuration.

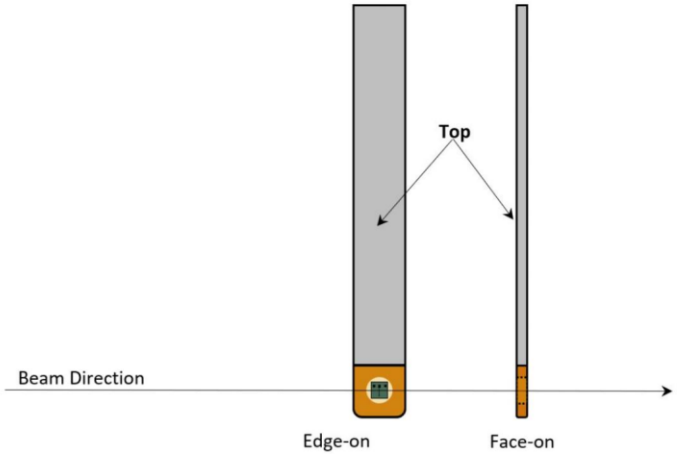

Figure 1. Schematic representation of the EPI37 detector chip (0.75 × 1.0 mm^2, shown in green) integrated in the patented CMRP "drop-in" configuration within a 10 mm-wide Kapton pigtail (brown) with aluminium radio frequency (RF) shielding (grey). For the measurements presented in this work, the detector was operated in both edge-on and face-on orientations with respect to the incident beam direction, as indicated in the diagram.

2. Materials and Methods

2.1. EPI37 Device Architecture

The EPI37 diode structure was fabricated through ion implantation within a 37 µm thick, 100 Ω·cm p-type epitaxial silicon layer, which is grown upon a 300 µm thick low resistivity (0.001 Ω·cm) p-type substrate. The detector employs a PNP solid-state architecture, in which a central n^+-doped sensitive region is enclosed by p^+-doped regions. When appropriately biased, an electric field is established across the depletion region, enabling efficient collection of radiation-induced charge carriers. The single strip (n-type) dimensions are 5 µm × 200 µm. A 10 µm-wide, n-type guard ring surrounds the strip with a spacing between strip and guard ring of 5 µm, see Figure 2. A layer of SiO_2 surrounds the diode structure to protect the device from unwanted contaminants and reduce surface leakage currents. The area directly below the aluminium contact pads forms a Metal-Oxide-Semiconductor structure, where the field oxide limits the electric field in this region of the device.

The EPI37 topology includes the guard ring to help minimise the collection of charge resulting from interactions in the device outside of the sensitive volume. This is accomplished by the collection of charge produced outside the sensitive volume by the guard ring, effectively shielding the n^+ strip. The subsequent effect of this implementation is an improved spatial resolution of the device when used in a face-on configuration, with the caveat of a decreased sensitivity of the device.

For charge collection characterisation, a total of six devices were mounted onto a standard 20-pin Dual In-Line package; while for MRT dosimetry, SSDs were mounted onto a purpose-made 600 µm thick, 10 mm wide, and 300 mm long Kapton probe [15], using 'Drop-In' technology. This patented Drop-In technology [29,30] is flexible and minimises dose enhancement caused by the surrounding materials, common with commercial components (Figure 3). This packaging enables the use of the EPI37 within both solid and liquid water phantoms without the need for an additional waterproof sleeve, bolstering the versatility of the device for routine QA measurements.

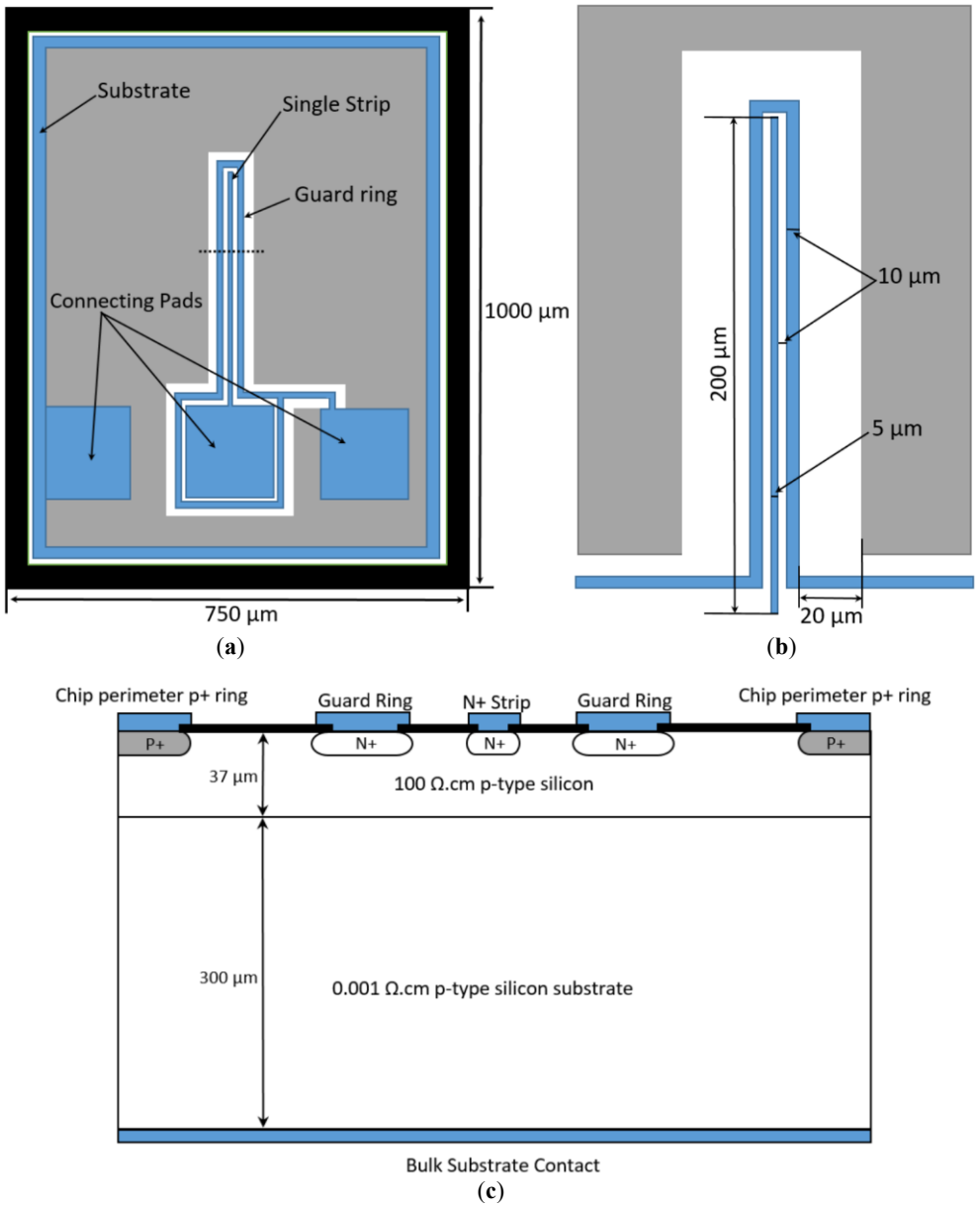

Figure 2. (**a**) Top view of the EPI37 detector. (**b**) Magnified view of the EPI37 sensitive volume strip. (**c**) Cross-sectional view of the sensitive strip along the dotted line indicated in (**a**), illustrating the layered structure of the device. Grey regions correspond to the SiO_2 layer, and blue regions indicate aluminium contact pads.

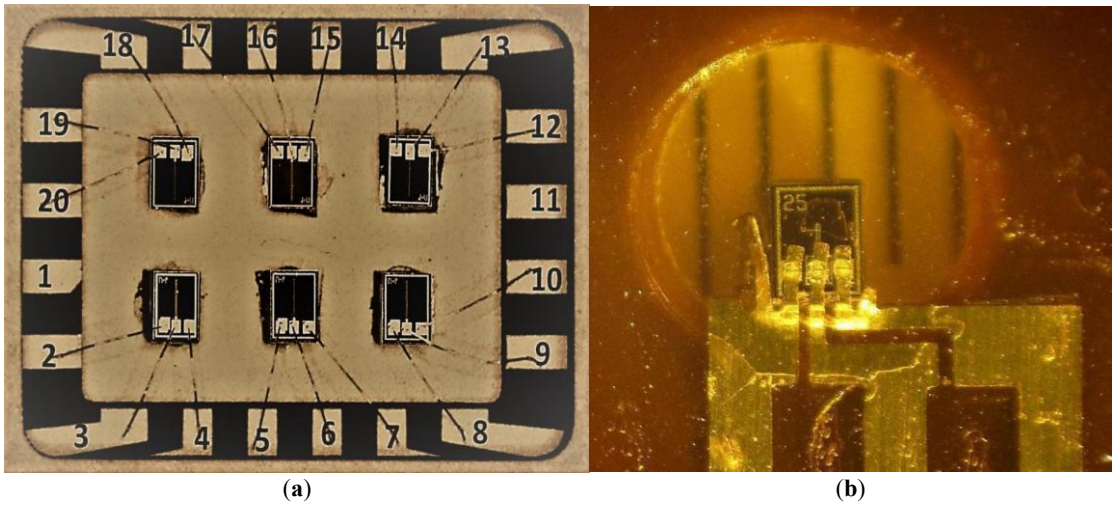

Figure 3. (**a**) EPI37 mounted on a 20-pin Dual In-Line package. (**b**) Close-up of EPI37 mounted using Drop-In technology on Kapton probe.

2.2. Ion Beam Induced Charge Microscopy

The Charge Collection Efficiency (CCE) of the EPI37 detector was characterised at the SIRIUS microprobe facility, Australian Nuclear Science and Technology Organisation, using the Ion Beam Induced Charge collection (IBIC) technique [31]. Experiments employed 5.5 MeV He^{2+} ions, which have an approximate penetration depth of 28 μm in silicon [32]. The ion beam was focused to a sub-micrometre spot size [32] and raster-scanned across the sample surface at normal incidence, with a constant particle flux of approximately 1000 ± 100 ions/s to ensure consistency.

The scanned region was divided into a 256 × 256 pixel map, with each pixel measured for 500 μs. An Ortec 142 charge-sensitive pre-amplifier collected the induced charge signal at the n^+ electrode, generated by incoming charge carriers. The signal was shaped using a 1-μs shaping amplifier and then analysed by a multi-channel analyser (MCA). The MCA sorts the signals into energy bins and records data via a dedicated data acquisition (DAQ) system. The DAQ's time constant was optimised based on the ion rate to distinguish individual ion impact events effectively.

For each (x, y) coordinate, the charge was collected, with the signal amplitude directly related to the energy deposited (ΔE) during the ion's passage. To convert the measured signal to energy, a calibration was performed using a 300 μm thick, windowless Hamamatsu silicon PIN diode (S3590-09), with known 100% CCE. A pulse generator mimicked the signal the diode would produce for known energy depositions, allowing the creation of an energy calibration curve. Custom MATLAB scripts were utilised to generate the measured MCA spectrum and median energy maps across the scanned region.

The device's CCE was evaluated by comparing the maximum energy detected in the MCA spectrum with the theoretical energy deposition predicted by SRIM simulations [33]. The charge collection depth of the EPI37 was estimated by utilising the SRIM code to determine the theoretical range of He^{2+} ions in silicon that would correspond to the maximum measured energy in the MCA spectrum. The theoretical range of He^{2+} ions with this energy was assumed to correlate to the charge collection depth, and consequently, the expected spatial resolution when the EPI37 is used in edge-on mode.

The following bias configurations were tested, with applied bias voltages ranging from 0–40 V:

- Positive bias applied to the n^+ electrode with the guard ring disconnected
- Positive bias applied to both the guard ring and the n^+ electrode
- No bias applied to either the guard ring or n^+ electrode (passive mode)

2.3. Australian Synchrotron Measurements

EPI37 devices mounted on Kapton probes were evaluated at the IMBL at the Australian Synchrotron, within Experimental Hutch 2B, using both face-on and edge-on configurations. For edge-on measurements, the guard ring was disconnected and the strip held at 0 V. In contrast, face-on measurements were conducted with both the guard ring and strip biased at 20 V. For comparison, measurements using the previous-generation detector, the EPI50 [24,25], were limited to face-on operation, with both the strip and guard ring biased at 50 V. This configuration restricted the sensitive volume width to approximately 30 μm [15], corresponding to the highest spatial resolution mode of the detector.

The vertical dimension of the synchrotron-generated X-ray beam at the IMBL was defined using interchangeable tungsten beam-defining apertures (BDAs). In this study, the selected BDA produced an intrinsic beam propagating in the +X direction, with a width of 30 mm and a height of 2.014 mm (Figure 4). To further refine the beam geometry, a tungsten conformal mask was positioned approximately 0.5 m downstream of the BDA, producing a final intrinsic beam size of 20 mm × 2.014 mm (Y, Z). This conformal mask was mounted on a motorised sample stage that moved synchronously with the water phantom. To define the intrinsic microbeam field, the MSC, as illustrated in Figure 4, was remotely positioned into the beam path. The remote insertion of the MSC facilitates reproducibility and minimised manual intervention, which is critical for maintaining beam line alignment and dosimetric accuracy during experimental procedures.

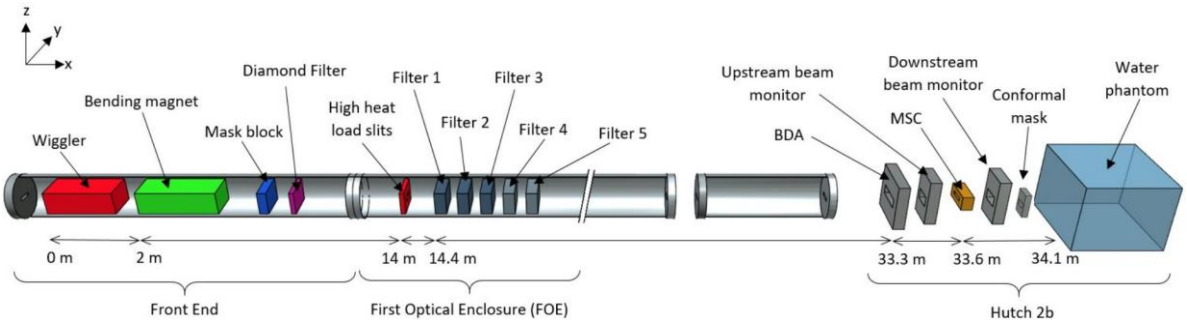

Figure 4. Schematic of the IMBL beamline, reproduced from [20].

Insertion of the MSC located in Hutch 2B, produces an array of vertical microbeams. The MSC has physical dimensions of 8 × 40 × 8 mm³ (X, Y, Z) and comprises 125 individual slits, each with a width of 50 μm and c-t-c spacing of 400 μm. A summary of the beam line parameters and configuration employed for all experimental measurements at the IMBL is presented in Table 1.

Table 1. Beamline configuration for experimental measurements at the IMBL. The thickness presented for each of the filters implemented on the IMBL is given as the effective thickness seen by the beam, accounting for geometry and rotation. * Based on Geant4 simulations [20].

Parameter	Value
Storage ring current	200.3 mA
Storage ring electron energy	3.032 GeV
Source to phantom surface distance	34 m
Peak wiggler magnetic field strength	3 T
Beamline Filtration	0.45 mm graphene +7.07 mm HD graphite +14.14 mm HD graphite +1.41 mm Cu +1.41 mm Cu
Mean Photon Energy	92 keV *

Given the maximum intrinsic beam dimensions of 2 mm height and 30 mm width, clinically relevant treatment fields were generated by translating the phantom through the beam at a constant speed, as illustrated in Figure 5. For this study, the phantom stage was translated at a vertical speed of 10 mm/s, resulting in a 20 × 20 mm² field at the phantom surface, defined by the tungsten conformal mask.

All measurements were performed in a water phantom with physical dimensions of 140 × 100 × 100 mm³ (X, Y, Z). Fine positioning of the detector in depth (Z) was achieved using a dedicated stepper motor. The phantom was mounted on a motorised sample stage located approximately 34 m from the X-ray source, inside Hutch 2B.

Each detector was aligned within the beam field prior to measurement. Initial alignment was carried out using in-room lasers, followed by fine adjustments using planar X-ray imaging to accurately position the sensitive volume.

Both intrinsic and treatment beam profiles were acquired using the EPI37 to evaluate performance under each measurement condition. The intrinsic microbeam profile was characterised at a depth of 20 mm in the water phantom using both the EPI37 and EPI50 detectors. Each device's sensitive volume was aligned to the centre of the microbeam array, then laterally offset by 15 mm along the Y-axis. The sample stage was translated 30 mm horizontally (X) at a constant speed of 4 mm/s. Online signal acquisition was performed using the X-TREAM readout system [15].

Treatment field profiles were also acquired using the PTW microDiamond and EPI37 detectors, with signal acquisition via the PTW Webline electrometer. A custom BNC-to-USB cable was developed to interface the electrometer with the EPI37. The PTW microDiamond was operated in passive mode (i.e., no external bias), in accordance with manufacturer specifications.

A central axis Y-profile of a 20 mm × 20 mm treatment field was obtained using a step-and-scan (SnS) procedure. The detector was initially aligned to the centre of the conformal mask aperture, then offset by −0.8 mm in Y and −12 mm in Z. The stage was then translated vertically by 24 mm at a constant speed of 10 mm/s. Following each vertical scan, the detector position was reset and shifted laterally by +10 μm. This process was repeated until the Y-position reached +0.8 mm, yielding a central axis Y-profile encompassing the central microbeams. A high-

resolution scan of the central microbeam was then performed using the same procedure with a lateral step size of 1 µm.

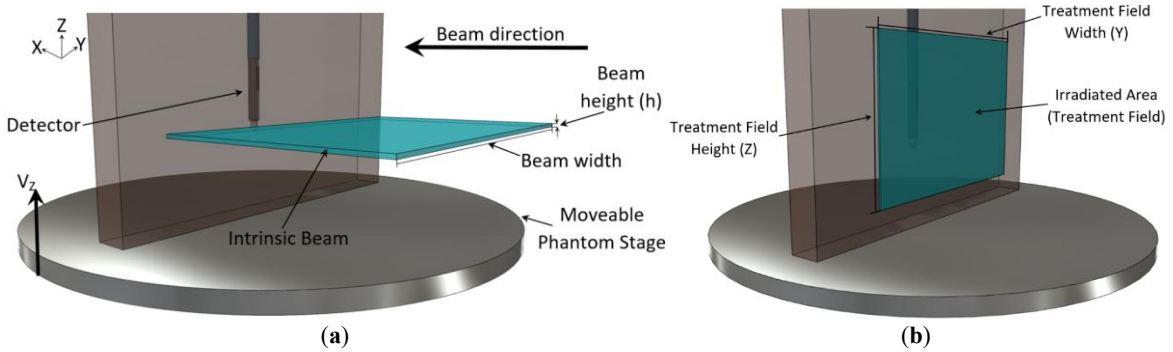

Figure 5. Illustration of (**a**) the intrinsic field and (**b**) the treatment field.

The entire measurement process was automated via a custom Python script, which interfaced with the motorised sample stage, beamline controls, electrometer, and phantom positioning system. For comparison, the SnS procedure was repeated using the EPI37 in edge-on mode, with 0 V applied to the strip and the guard ring disconnected.

3. Results

3.1. Ion Beam Induced Charge Microscopy

The MCA spectrum and associated median energy maps, where the EPI37 is operated with the guard ring floating and voltages applied to the n^+ strip of 0, 15, and 40 V are depicted in Figures 6–8, respectively.

Figure 9 depicts the MCA spectrum and associated median energy maps where the EPI37 is operated with the guard ring connected and both the guard ring and n^+ strip biased with 20 V.

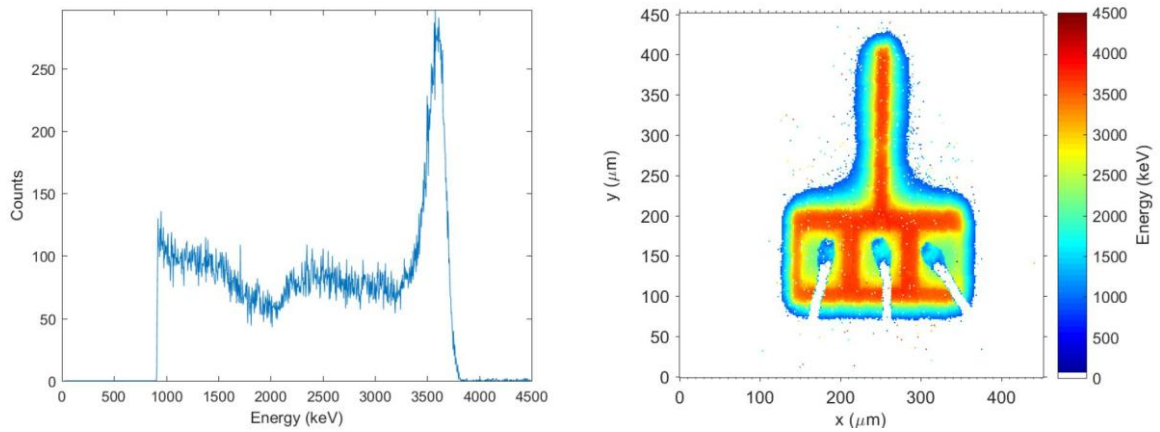

Figure 6. (**a**) MCA spectrum and (**b**) median energy map, for EPI37 when operated in passive mode and guard ring floating.

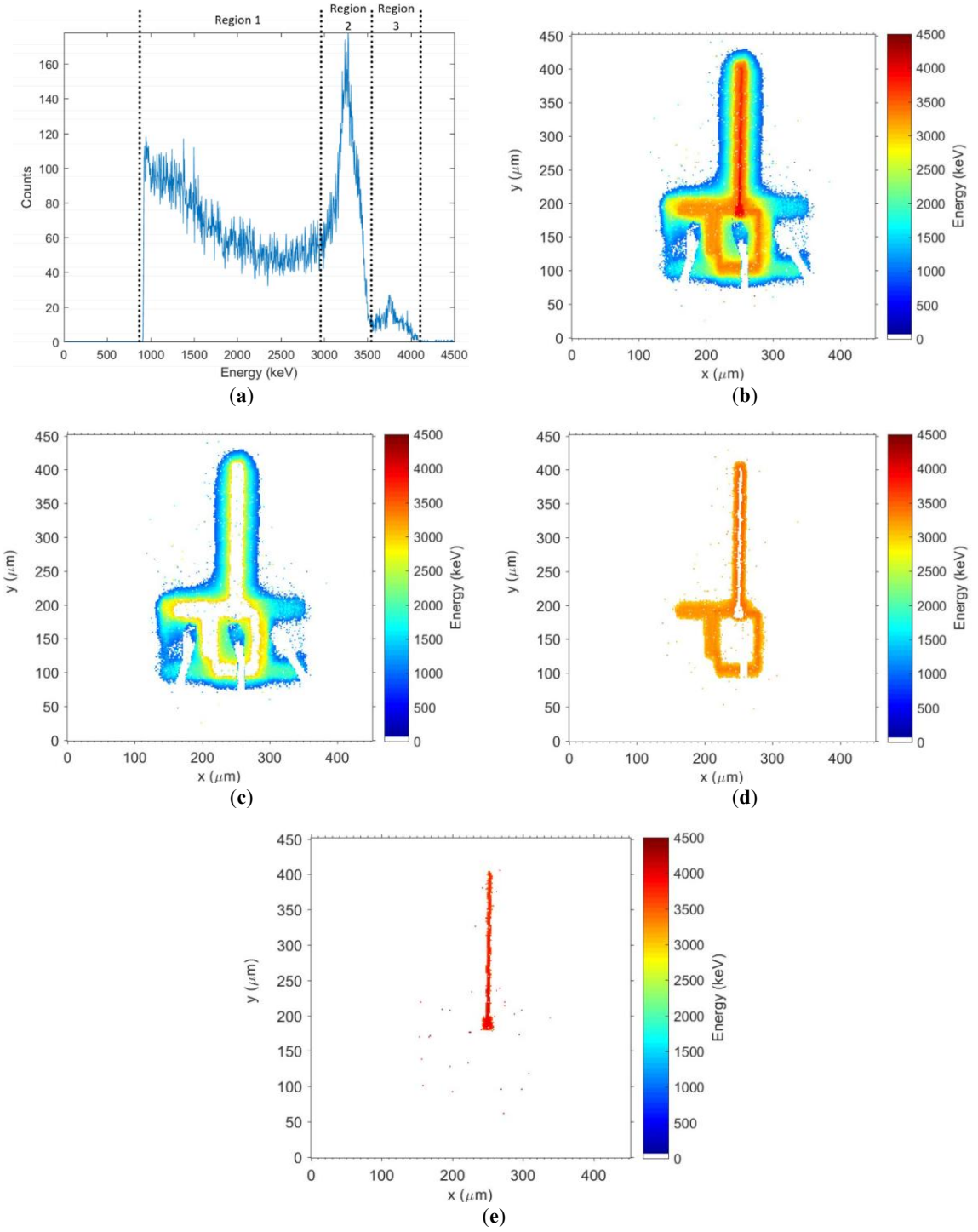

Figure 7. (**a**) MCA spectrum and (**b**) median energy map, for EPI37 with strip biased at 15 V and guard ring floating. MCA spectrum generated from (**c**) Region 1, (**d**) Region 2, and (**e**) Region 3.

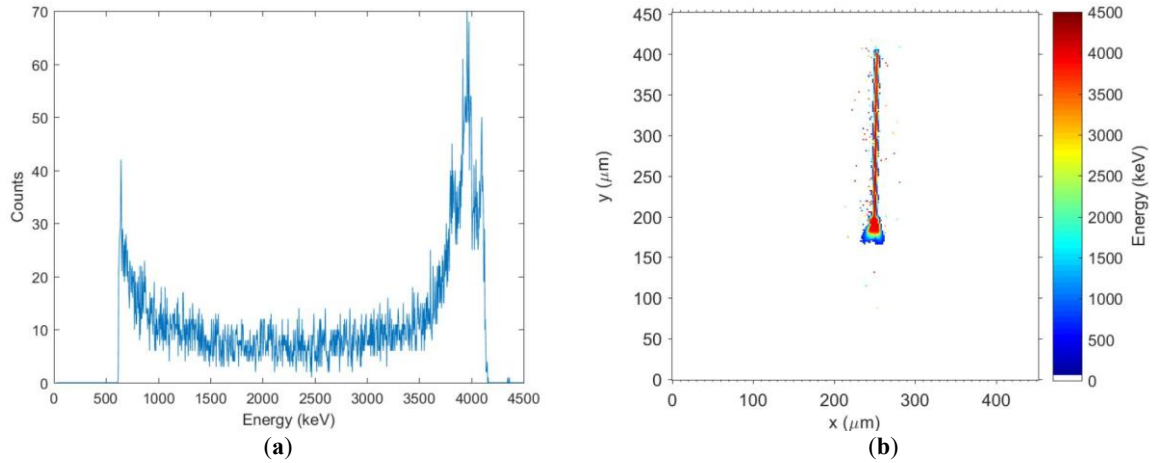

(**a**) (**b**)

Figure 8. (**a**) MCA spectrum and (**b**) median energy map, for EPI37 with strip biased at 40 V and guard ring floating.

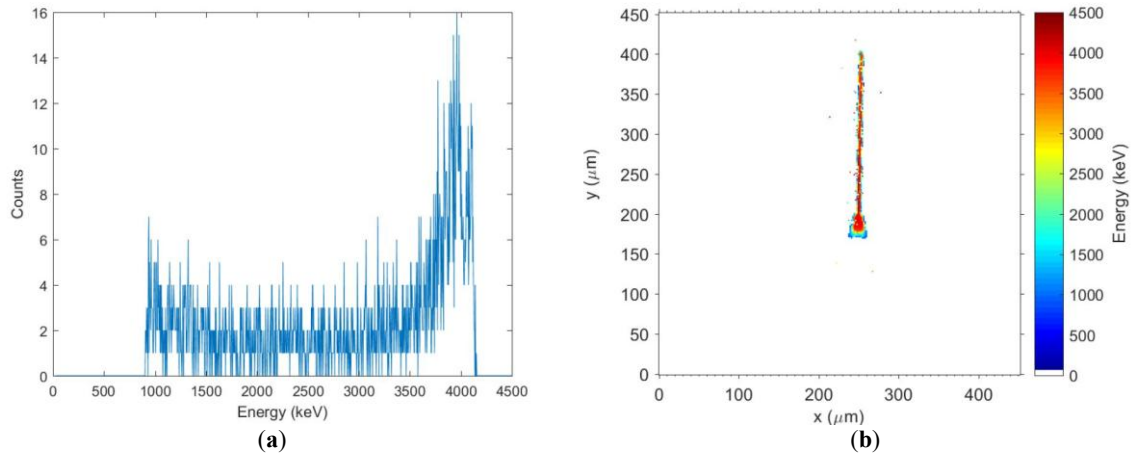

(**a**) (**b**)

Figure 9. (**a**) MCA spectrum and (**b**) median energy map, for EPI37 with both strip and guard ring biased at 20 V.

3.2. Australian Synchrotron Measurements

The central microbeams of an intrinsic microbeam profile, obtained at the IMBL using the EPI37 in both face-on and edge-on configurations, are shown in Figure 10. The average FWHM of the measured intrinsic microbeam profiles, as shown in Figure 10, was (50.5 ± 1.4) μm and (46.4 ± 1.9) μm for the edge-on and face-on orientations, respectively.

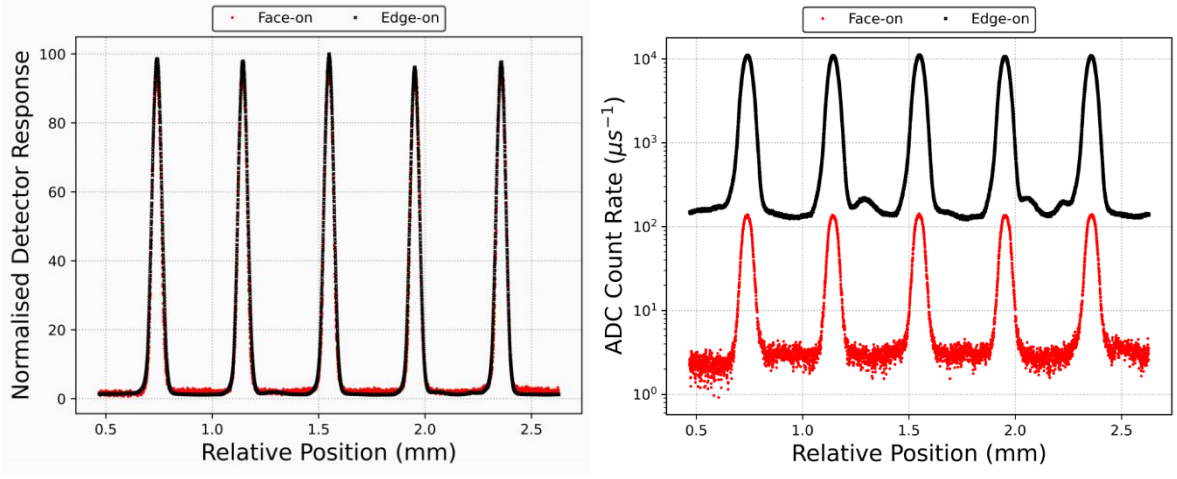

(**a**) (**b**)

Figure 10. Overlay of central five microbeams measured with EPI37 in an edge-on or face-on configuration with (**a**) normalised detector response and (**b**) absolute detector response.

A region encompassing the central microbeams of an intrinsic MRT profile, obtained at the IMBL using the EPI37 in an edge-on configuration and the EPI50 in a face-on configuration, is shown in Figure 11. The average FWHM of the measured intrinsic microbeam profiles was (50.5 ± 1.4) µm for the EPI37 and (62.8 ± 1.3) µm for the EPI50.

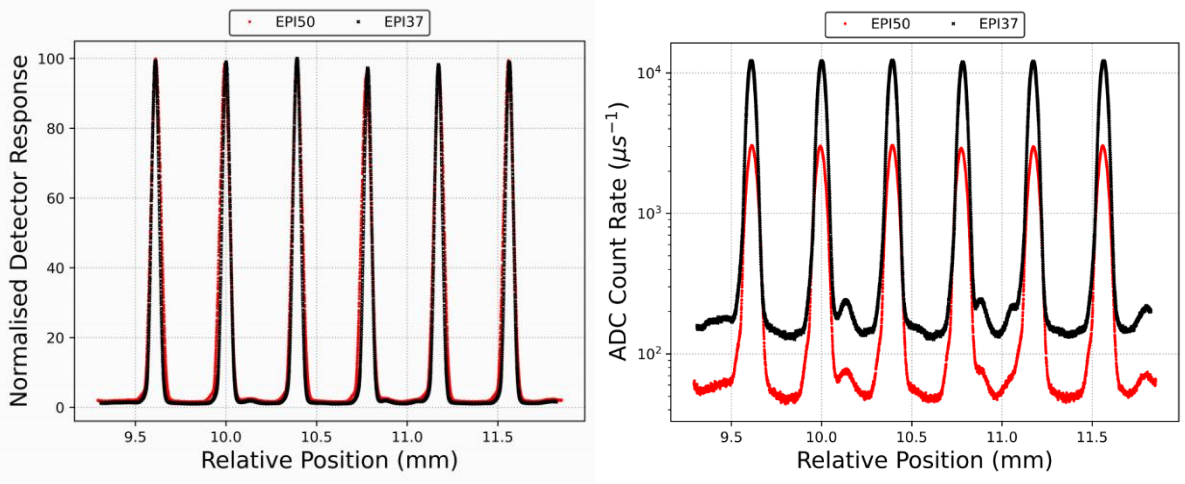

(**a**) (**b**)

Figure 11. Overlay of (**a**) normalised detector response and (**b**) absolute detector response, for the central microbeams measured with EPI37 in an edge-on configuration and the EPI50 in a face-on configuration.

The central axis treatment field Y-profiles for the central microbeams, measured with both the PTW microDiamond and EPI37 for step sizes of 5 µm and 1 µm, are depicted in Figure 12.

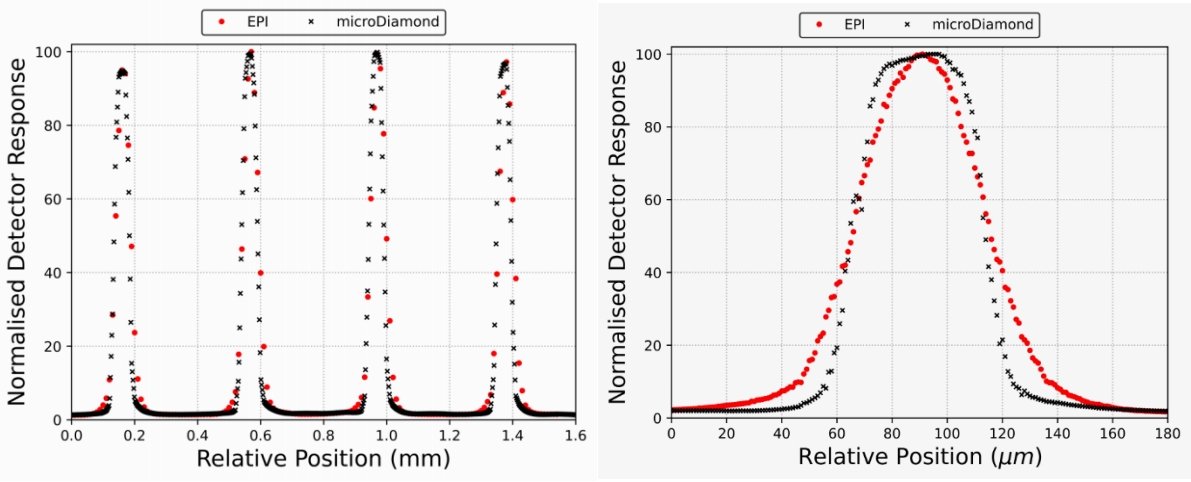

(**a**) (**b**)

Figure 12. (**a**) Central microbeams measured with EPI37 and microDiamond in an edge-on configuration, with a 5 µm and 1 µm step length, respectively. (**b**) Central microbeam measured with EPI37 and microDiamond in an edge-on configuration, with a 1 µm step length.

A summary of the key microbeam characteristics for the central microbeams measured with the EPI37 and PTW microDiamond is presented in Table 2.

Table 2. Summary of dosimetric characteristics for the central microbeams of a 20 mm × 20 mm MB field at a depth of 20 mm in a water phantom, determined by the EPI37 and microDiamond detectors using a SnS methodology. The uncertainties are represented by one standard deviation of the mean.

Parameter	EPI37	microDiamond
Mean PVDR	48	44
Mean FWHM of central microbeam (µm)	51.4 ± 1.2	49.7 ± 0.9

4. Discussion

The two operational configurations of the EPI37 device were investigated using 5.5 MeV alpha particles, following the IBIC methodology [32]. In this study, the central strip was positively biased in the range of 0–40 V, with the guard ring either biased at the same potential as the central strip or left floating.

Figure 6 shows the device operating in passive mode. In this configuration, no charge shielding from the guard ring is observed, and charge is collected over a large area encompassing both the strip and guard ring.

When a bias of 15 V is applied to the central strip with the guard ring disconnected, the charge collection by the central strip decreases at the lateral edges of the device, particularly near the guard ring and p^+ pads, as seen in Figure 7. This is likely due to increased recombination of minority carriers in the substrate. To further investigate the origins of charge collection under these bias conditions, median energy maps were generated for three manually defined regions of interest, centered on distinct features of the MCA spectrum (Figure 7a). A distinct high-energy peak with reduced collection rate is evident under these conditions, as shown in the median energy map of Region 3 in Figure 7e. The reduction in signal from charge carriers outside the depletion region, due to recombination in the substrate, facilitates differentiation of the charge carriers confined to the geometric bounds of the strip and surrounding materials.

As the bias applied to the strip increases, charge collection becomes increasingly localised to the strip's geometric dimensions, as seen in Figure 8. At approximately 30 V, a notable reduction in device sensitivity is observed. Furthermore, higher bias increases the maximum collected energy, corresponding to a deeper charge collection depth within the device. This reduces the expected spatial resolution in edge-on configurations. Therefore, passive-mode operation is recommended for edge-on applications, as the transverse charge isolation provided by the guard ring is unnecessary and only degrades sensitivity.

The results presented in Figure 9 demonstrate that, in face-on operation, connecting the guard ring effectively confines charge collection to the strip's geometric area. However, this configuration results in a marked reduction in sensitivity, potentially limiting its use to high-dose-rate applications. At higher bias, a modest improvement in spatial resolution is achieved, at the cost of further loss in sensitivity. At 20 V bias, the SV width was measured to be (12.1 ± 0.5) μm, decreasing to approximately (10.8 ± 0.3) μm at 40 V. Therefore, for face-on operation, a bias of 20 V applied to both the strip and guard ring is recommended (Figure 9). This behaviour allows the device configuration to be optimised for specific measurement requirements. Notably, an expansion of the charge collection area is observed at the lower end of the strip, likely caused by local electric field enhancement due to the strip's connection geometry [26], leading to a maximum lateral SV width of 22 μm at 20 V.

The low charge collection efficiency observed suggests that the SV depth is smaller than the 37 μm epitaxial layer thickness, and that the guard ring collects charge from beneath the SV. The estimated collection depths are 22 μm and 19 μm for face-on and edge-on configurations, respectively.

The central microbeams of an intrinsic microbeam profile, measured at the IMBL using the EPI37 in both face-on and edge-on configurations, are shown in Figure 10. The face-on configuration exhibits a substantial reduction in signal-to-noise ratio compared to edge-on operation, particularly in the valley regions where the signal approaches baseline noise.

The FWHM measured with the EPI37 in a face-on configuration and in an edge-on configuration were (46.4 ± 1.9) μm and (50.5 ± 1.4) μm, respectively (Figure 10). The lower-than-expected FWHM measured by the EPI37 when utilised in a face-on configuration suggests the guard ring may be having an undesirable effect and should be investigated further. This effect may be similar to that observed in the IBIC observations (Figure 9), which appears to be mitigated at high dose rates, which saturate the guard ring and allow effective charge collection by the strip.

Based on the reduced signal-to-noise ratio in the valley regions of face-on operation and the lack of significant improvement in spatial resolution, it is recommended that the device be used in an edge-on configuration. Face-on operation may only be suitable in high dose-rate conditions, where edge-on operation risks readout saturation.

The central intrinsic microbeams of an MRT profile, measured using the EPI37 in an edge-on configuration and EPI50 in a face-on configuration, are shown in Figure 11. The measured FWHM was (50.5 ± 1.4) μm and (62.8 ± 1.3) μm for the EPI37 and EPI50, respectively. This demonstrates the improved spatial resolution of the EPI37. This improvement supports the conclusion that charge collection in the EPI37's 37 μm epitaxial layer is confined to a narrower 19 μm depth, consistent with IBIC characterisation. Additionally, the EPI37 exhibited higher signal-to-noise than the earlier-generation EPI50.

A summary of microbeam characteristics measured with the EPI37 and PTW microDiamond (Figure 12) is provided in Table 2. A 9% difference in the mean peak-to-valley dose ratio was observed, attributed to the 8% higher mean valley response measured by the microDiamond relative to the EPI37. The source of the discrepancies

in the PVDR remains unresolved, due to the complex interplay of factors such as scattered radiation response, beamline configuration, detector characteristics, and readout uncertainties. Identifying a suitable detector thus remains an ongoing challenge.

The FWHM was determined using the finer 1 μm SnS of the central microbeam, due to the limited data points in the coarse 5 μm-resolution scans. The FWHM measurements from the EPI37 and microDiamond agreed, within experimental uncertainty, with the expected microbeam width. This agreement is promising and suggestive of the potential use of the EPI37 as a QA detector for relative dosimetry in MRT applications; however, a more comprehensive dosimetric evaluation of the EPI37 performance is required.

5. Conclusions

CMRP has developed a next-generation p-type epitaxial-based SSD for QA in synchrotron MRT. The detector's charge collection characteristics have been extensively investigated using the IBIC methodology. The expected spatial resolution of EPI37 in an edge-on configuration was determined to be 19 μm while operated in passive mode. When used in a face-on configuration, 20 V bias is recommended to be applied to both the guard ring and n^+ strip. Under these biased conditions, the expected spatial resolution of the detector is 22 μm.

Measurements of intrinsic microbeam profiles at the Australian Synchrotron demonstrated improvements in both spatial resolution and sensitivity compared to the previous generation EPI50. In edge-on orientation, the EPI37 exhibited enhanced sensitivity while maintaining comparable spatial resolution to face-on operation. However, the significant reduction in sensitivity in face-on mode suggests its application should be utilised when the response in edge-on mode demonstrates saturation.

The reduced impact of geometric positioning on the spatial resolution of the EPI37 relative to the PTW microDiamond further supports its practical utility in routine workflows. Comparative measurements between the commercially available PTW microDiamond and EPI37 suggest the suitability of the EPI37 for measurements of pertinent characteristics of MRT fields, such as PVDR and FWHM. Future work performing a thorough dosimetric evaluation of the EPI37 is required to confirm the suitability of the EPI37 detector for relative dosimetry of MRT fields.

Author Contributions

Conceptualization: A.D., M.P. and A.B.R.; Methodology: A.D., J.A.D., V.P. and M.P.; Data analysis: A.D. and J.A.D.; Writing—original draft preparation: A.D. and J.A.D.; Writing—reviewing and editing: A.D., J.A.D., J.P., M.J.C., M.P., A.B.R. and M.L.F.L.; Supervision: J.A.D. and M.L.F.L.; Investigation: A.D., J.A.D., J.P., M.J.C., M.L.F.L. and Z.P.; Experimental characterization: A.D., J.A.D., J.P., M.J.C. and M.L.F.L.; Formal analysis: A.D., J.A.D., J.P., M.J.C., M.P., A.B.R. and M.L.F.L.; Interpretation of data: A.D., J.A.D., J.P., M.J.C., M.P., A.B.R. and M.L.F.L.; Resources: Z.P. and V.P.; Software: M.P.; Project administration: M.L.F.L. All authors have read and agreed to the published version of the manuscript.

Funding

This work was supported in part by the National Health and Medical Research (Grant No. APP1093256).

Institutional Review Board Statement

Not applicable.

Data Availability Statement

The data supporting the findings of this study are available upon reasonable request from the corresponding author. Due to the nature of the experimental setup and proprietary aspects of the single silicon strip detector fabrication, some data may be subject to institutional restrictions. All reasonable efforts will be made to ensure accessibility of the data to qualified researchers for at least 10 years following publication, in accordance with the journal policy.

Acknowledgments

This article is dedicated to the lifetime scientific contribution of Vladimir Perevertaylo, who tragically passed away from COVID-19. All authors declare that they have no known conflicts of interest in terms of competing financial interests or personal relationships that could have an influence or are relevant to the work reported in this article. The authors acknowledge the National Collaborative Research Infrastructure Strategy funding provided by the Australian Government for this research performed on the Sirius 6 MV tandem accelerator at Australian

Nuclear Science and Technology Organisation and the Imaging and Medical Beam Line at Australian Synchrotron. We also acknowledge the financial support of the National Health and Medical Research Council under the proposal application APP1093256 and the Australian Nuclear Science and Technology Organisation under the proposal RPP10102. This research has been conducted with the support of the Australian Government Research Training Program Scholarship.

Conflicts of Interest

The authors declare no conflict of interest.

References

1. Uyama, A.; Kondoh, T.; Nariyama, N.; et al. A narrow microbeam is more effective for tumor growth suppression than a wide microbeam: An in vivo study using implanted human glioma cells. *J. Synchrotron Radiat.* **2011**, *18*, 671–678.
2. Fernandez-Palomo, C.; Brauer-Krisch, E.; Laissue, J.; et al. Use of synchrotron medical microbeam irradiation to investigate radiation-induced bystander and abscopal effects *in vivo*. *Phys. Medica* **2015**, *31*, 584–595.
3. Bronnimann, D.; Bouchet, A.; Schneider, C.; et al. Synchrotron microbeam irradiation induces neutrophil infiltration, thrombocyte attachment and selective vascular damage *in vivo*. *Sci. Rep.* **2016**, *6*, 33601.
4. Engels, E.; Paino, J.R.; Vogel, S.E.; et al. Modulating synchrotron microbeam radiation therapy doses for preclinical brain cancer. *Radiation* **2023**, *3*, 183–202.
5. Winter, J.; Galek, M.; Matejcek, C.; et al. Clinical microbeam radiation therapy with a compact source: Specifications of the line-focus X-ray tube. *Phys. Imaging Radiat. Oncol.* **2020**, *14*, 74–81.
6. Petrich, C.; Winter, J.; Dimroth, A.; et al. The compact line-focus X-ray tube for microbeam radiation therapy—Focal spot characterisation and collimator design. *Phys. Med.* **2025**, *129*, 104861.
7. Matejcek, C.; Winter, J.; Aulenbacher, K.; et al. A novel electron source for a compact X-ray tube for microbeam radiotherapy with very high dose rates. *Phys. Med.* **2023**, *106*, 102532.
8. Bravin, A.; Olko, P.; Schültke, E.; et al. Syra3 cost action—Microbeam radiation therapy: Roots and prospects. *Phys. Med.* **2015**, *31*, 561–563.
9. Grotzer, M.A.; Schultke, E.; Brauer-Krisch, E.; et al. Microbeam radiation therapy: Clinical perspectives. *Phys. Med.* **2015**, *31*, 564–567.
10. Griffin, R.J.; Koonce, N.A.; Dings, R.P.M.; et al. Microbeam radiation therapy alters vascular architecture and tumor oxygenation and is enhanced by a galectin-1 targeted anti-angiogenic peptide. *Radiat. Res.* 2012. 177, 804–812.
11. Engels, E.; Li, N.; Davis, J.; et al. Toward personalized synchrotron microbeam radiation therapy. *Sci. Rep.* **2000**, *10*, 8833.
12. Accuracy Requirements and Uncertainties in Radiotherapy. Human Health Series. Vienna: International Atomic Energy Agency. 2016. Available online: https://www.iaea.org/publications/10668/accuracy-requirements-and-uncertainties-in-radiotherapy (accessed on 8 June 2025).
13. Davis, J.A.; Engels, E.; Petasecca, M.; et al. X-tream protocol for in vitro microbeam radiation therapy at the Australian Synchrotron. *J. Appl. Phys.* **2021**, *129*, 244902.
14. Paino, J.; Barnes, M.; Engels, E.; et al. Incorporating clinical imaging into the delivery of microbeam radiation therapy. *Appl. Sci.* **2021**, *11*, 9101.
15. Petasecca, M.; Cullen, A.; Fuduli, I.; et al. X-tream: A novel dosimetry system for synchrotron microbeam radiation therapy. *J. Instrum.* **2012**, *7*, P07022.
16. Br, E.; Serduc, R.; Siegbahn, E.; et al. Effects of pulsed, spatially fractionated, microscopic synchrotron X-ray beams on normal and tumoral brain tissue. *Mutat. Res.* **2010**, *704*, 160–166.
17. Lillicrap, S.C. Physics aspects of quality control in radiotherapy (Report No. 81). *Phys. Med. Biol.* **2000**, *45*, 815.
18. Bartzsch, S.; Lott, J.; Welsch, K.; et al. Micrometer-resolved film dosimetry using a microscope in microbeam radiation therapy. *Med. Phys.* **2015**, *42*, 4069–4079.
19. Ocadiz, A.; Livingstone, J.; Donzelli, M.; et al. Film dosimetry studies for patient specific quality assurance in microbeam radiation therapy. *Phys. Med.* **2019**, *65*, 227–237.
20. Dipuglia, A.; Cameron, M.; Davis, J.A.; et al. Validation of a Monte Carlo simulation for microbeam radiation therapy on the imaging and medical beamline at the Australian Synchrotron. *Sci. Rep.* **2019**, *9*, 17696.
21. Livingstone, J.; Stevenson, A.W.; Butler, D.J.; et al. Characterization of a synthetic single crystal diamond detector for dosimetry in spatially fractionated synchrotron X-ray fields. *Med. Phys.* **2016**, *43*, 4283.
22. Davis, J.; Petasecca, M.; Cullen, A.; et al. X-tream dosimetry of synchrotron radiation with the PTW microDiamond. *J. Instrum.* **2019**, *14*, P10037.

23. Lerch, M.L.F.; Dipuglia, A.; Cameron, M.; et al. New 3D Silicon detectors for dosimetry in Microbeam Radiation Therapy. *J. Phys. Conf. Ser.* **2017**, *777*, 012009.
24. Fournier, P.; Cornelius, I.; Donzelli, M.; et al. X-tream quality assurance in synchrotron X-ray microbeam radiation therapy. *J. Synchrotron Radiat.* **2016**, *23*, 1180–1190.
25. Fournier, P.; Cornelius, I.; Dipuglia, A.; et al. X-tream dosimetry of highly brilliant X-ray microbeams in the MRT hutch of the Australian Synchrotron. *Radiat. Meas.* **2017**, *106*, 405–411.
26. Davis, J.A.; Paino, J.R.; Dipuglia, A.; et al. Characterisation and evaluation of a PNP strip detector for synchrotron microbeam radiation therapy. *Biomed. Phys. Eng. Express* **2018**, *4*, 044002.
27. Davis, J.; Dipuglia, A.; Cameron, M.; et al. Evaluation of silicon strip detectors in transmission mode for online beam monitoring in microbeam radiation therapy at the Australian Synchrotron. *J. Synchrotron Radiat.* **2022**, *29*, 29–41.
28. Duncan, M.; Donzelli, M.; Pellicioli, P.; et al. First experimental measurement of the effect of cardio-synchronous brain motion on the dose distribution during microbeam radiation therapy. *Med. Phys.* **2020**, *47*, 213–222.
29. Rozenfeld, A. B. “Radiation Sensor and Dosimeter”. China Patent CN101730535B, authorized 2 June 2008. Rozenfeld, A.B. Radiation Detector and Dosimeter. U.S. Patent US8742357B2, 2014.
30. Breese, M.B.H. A theory of ion beam induced charge collection. *J. Appl. Phys.* **1993**, *74*, 3789–3799.
31. Pastuovic, Z.; Davis, J.; Tran, T.L.; et al. IBIC microscopy—The powerful tool for testing micron-sized sensitive volumes in segmented radiation detectors used in synchrotron microbeam radiation and hadron therapies. *Nucl. Instrum. Methods Phys. Res. Sect. B Beam Interact. Mater. At.* **2019**, *458*, 90—96.
32. Ziegler, J.F.; Ziegler, M.D.; Biersack, J.P. SRIM—The stopping and range of ions in matter (2010). *Nucl. Instrum. Methods Phys. Res. Sect. B Beam Interact. Mater. At.* **2010**, *268*, 1818–1823.